J. Fluid Mech. (2007), *vol.* 582, *pp.* 179–202.
doi:10.1017/S0022112007005770 Printed in the United Kingdom

Acoustic resonances in a high-lift configuration

STEFAN HEIN[1], THORSTEN HOHAGE[2], WERNER KOCH[1] AND JOACHIM SCHÖBERL[3]

[1]Institute of Aerodynamics and Flow Technology, DLR Göttingen, Germany
[2]Institute for Numerical and Applied Mathematics, University of Göttingen, Germany
[3]Centre for Computational Engineering Science, RWTH Aachen University, Germany

(Received 28 June 2006 and in revised form 17 January 2007)

Low- and high-frequency acoustic resonances are computed numerically via a high-order finite-element code for a generic two-dimensional high-lift configuration with a leading-edge slat. Zero mean flow is assumed, approximating the low-Mach-number situation at aircraft landing and approach. To avoid unphysical reflections at the boundaries of the truncated computational domain, perfectly matched layer absorbing boundary conditions are implemented in the form of the complex scaling method of atomic and molecular physics. It is shown that two types of resonance exist: resonances of surface waves which scale with the total airfoil length and longitudinal cavity-type resonances which scale with the slat cove length. Minima exist in the temporal decay rate which can be associated with the slat cove resonances and depend on the slat cove geometry. All resonances are damped owing to radiation losses. However, if coherent noise sources exist, as observed in low-Reynolds-number experiments, these sources can be enhanced acoustically by the above resonances if the source frequency is close to a resonant frequency.

1. Introduction

Through technological progress, such as ultra high bypass ratio turbofan engines and improved acoustical liners in the nacelle, aircraft engines of modern commercial airliners have become significantly quieter in the past four decades. With the efficient reduction of engine noise, airframe noise has emerged as an ever more important component of the overall aircraft noise, especially during aircraft approach and landing when the engines are at low power (Crighton 1991). Experimental studies on both sides of the Atlantic based on free-flight tests of production aircraft (Michel *et al.* 1998 (various aircraft); Piet, Michel & Böhning 2002 (Airbus A340); Stoker *et al.* 2003 (Boeing 777)), or wind-tunnel tests of scaled aircraft models (for example Grosche, Schneider & Stiewitt 1997 (Airbus A340); Hayes *et al.* 1997 (DC 10); Davy, Moens & Remy 2002 (Airbus A320/A321), Soderman *et al.* 2002 (Bombardier CRJ-700); Oerlemans & Sijtsma 2004 (Airbus A340); Horne *et al.* 2005 (Boeing 777)), have pinpointed high-lift devices and landing gears as dominant sources of airframe noise. In order to understand the noise source mechanisms better and find ways to reduce the noise emission, various aircraft components were investigated in more detail by advanced experimental and computational tools. Model-scale aeroacoustic tests on high-lift configurations such as Dobrzynski *et al.* (1998) (ALVAST high-lift model), Storms *et al.* (1999) (high-lift model), Khorrami, Berkman & Choudhari (2000) (high-lift model), Olson, Thomas & Nelson (2000) (high-lift model), Dobrzynski,

Gehlhar & Buchholz 2001 (Airbus A320 full-scale wing) or Dobrzynski & Pott-Pollenske (2001) (high-lift model), have identified the leading-edge slat as a major source of airframe noise. In addition to broadband noise, strong tones were observed under certain operating conditions in several of the above experiments. However, there is now general agreement that the observed low- to mid-frequency tones are due to model-scale Reynolds-number effects and full-scale slat flows are mostly broadband in character. Therefore, in order to simulate full-scale flight in wind-tunnel tests, boundary-layer tripping is usually employed on the upper and lower slat surface (see for example Andreou, Graham & Shin 2006; Fischer *et al.* 2006). Any evidence of low- to mid-frequency narrowband behaviour in full-scale tests can usually be traced to whistling caused by refuelling or vent holes (Czech *et al.* 2006), or other small-scale features such as slat tracks.

The above experiments and numerical studies performed mainly at NASA revealed two dominant slat noise sources, see the brief overview by Khorrami (2003): the tonal hump at high frequencies has been attributed to the finite thickness of the slat trailing edge. Using unsteady Reynolds-averaged Navier–Stokes simulations (URANS) with a high spatial resolution, Khorrami *et al.* (2000) were able to prove their conjecture that self-excited vortex shedding at the blunt trailing edge of the slat is the likely source for the tonal peak in the acoustic spectra at high frequencies. The vortex shedding at the trailing edge of the slat has since been confirmed by the experimental investigations of Olson *et al.* (2000) and Takeda, Zhang & Nelson (2002). Singer, Lockard & Brentner (2000) used the URANS data of Khorrami *et al.* (2000) to compute the acoustic far field by an acoustic analogy formulation based on the Ffowcs-Williams and Hawkings equation.

For the low-frequency noise, various source mechanisms have been proposed (Guo 1997; Olson, Thomas & Nelson 2001; Pott-Pollenske, Alvarez-Gonzalez & Dobrzynski 2003). As suggested by Storms *et al.* (1999), Roger & Pèrennés (2000) and Takeda *et al.* (2001), the convectively unstable separated shear layer in the slat cove can become self-excited by a feedback loop similar to the Rossiter modes in an open cavity (Rossiter 1964). To test this conjecture, Khorrami *et al.* (2002*a*) extended their two-dimensional URANS plus far-field computations to the slat cavity flow. The fully turbulent simulations proved overly diffusive and required explicit forcing of the shear layer to excite and maintain the large-scale structures. To circumvent the excessive diffusive effects of the turbulence model they used an *ad hoc* zonal approach in later versions (Khorrami *et al.* 2002*b*, 2004). With this, the shear layer became self-excited and qualitatively similar flow structures were found in the experiments of Takeda *et al.* (2001), Jenkins, Khorrami & Choudhari (2004) and Kaepernick, Koop & Ehrenfried (2005). To rectify remaining differences between the numerical and experimental results of Khorrami *et al.* (2004) and Jenkins *et al.* (2004), Choudhari & Khorrami (2006) extended their computations to include the effects of three-dimensional disturbances. Related three-dimensional simulations have been produced by Terracol *et al.* (2003) using a hybrid Reynolds-averaged Navier–Stokes simulation/large-eddy simulation (RANS/LES) method and by Deck (2005) employing a zonal detached eddy simulation. Choudhari & Khorrami (2006) and Deck (2005) showed encouraging comparisons between the computed and measured results.

The prominent peaks observed in the frequency spectra of several small-scale experiments (Dobrzynski *et al.* 1998; Pott-Pollenske *et al.* 2003; Roger & Pèrennés 2000), are now thought to be an artefact of low Reynolds number because no evidence was found in full-scale experiments such as Dobrzynski *et al.* (2001). Full-scale tests are costly and detailed wind-tunnel experiments will continue to be one

of the main sources of slat noise data. Therefore it is of importance to understand the limitations of these low-Reynolds-number wind-tunnel tests and why these tones occur. A better physical understanding of those tonal contributions may also allow us to circumvent these limitations in future experiments. One of the reasons behind these prominent narrowband tones might be an aeroacoustic feedback mechanism or enhancement of self-excited noise sources by acoustic resonances. The aeroacoustic feedback mechanism in the sense of the Rossiter mode physics is beyond the scope of this investigation. The present investigation concerns only acoustic resonances.

Storms *et al.* (1999) and Khorrami *et al.* (2000) have raised the question as to whether a feedback mechanism is operative in the gap between the slat and the main wing. This so-called gap resonance was investigated by Tam & Pastouchenko (2001) and Agarwal & Morris (2002) using a simple wall jet model. They conjectured that the shedding frequency at the slat trailing edge might be regulated by an acoustic feedback loop, when the shedding frequency matches one of the transverse resonance frequencies of the gap between the slat and the main wing, an intense tone is produced. Based on this feedback loop, Tam & Pastouchenko (2001) developed a simple formula for the gap tone frequency as a function of gap height, local flow speed and the local speed of sound. For a finite-length plate above a semi-infinite wall, Hein, Hohage & Koch (2004) showed that for zero flow, the one-dimensional gap resonances of Tam & Pastouchenko (2001) agree exactly with the least damped two-dimensional acoustic resonances. The gap resonances are resonances of transverse acoustic modes corresponding to the dominant modes in a simple two-mirror laser cavity. However, the slat cove resembles more a shallow open cavity than a laser cavity, and in a shallow cavity the longitudinal modes dominate (Koch 2005). This is probably why the frequencies computed via the simple acoustic feedback formula of Tam & Pastouchenko (2001) differed markedly from the experimental results of Takeda *et al.* (2002). Takeda, Zhang & Nelson (2004) extended the wall jet model of Tam & Pastouchenko (2001) to include the slat cove region using an idealized two-dimensional slat model. Performing a systematic variation of slat overlap and gap, their compressible URANS computations indeed indicated a strong influence of the slat/wing geometry on the high-frequency tones.

The objective of the present paper is the computation of acoustic resonances (also termed scattering frequencies) for a generic two-element high-lift system with a leading-edge slat in order to see if they are related in any way to the observed tones in low-Reynolds-number experiments. No account is taken of the underlying noise-generation mechanisms of these tones, and mean flow effects are neglected assuming that the acoustic resonances depend only weakly on Mach number. However, it should be pointed out that the noise sources in the form of unstable shear layers exist only if mean flow is present. Hein *et al.* (2004) argued that acoustic resonances in the high-lift system could provide a viable mechanism for the selection of a particular frequency: if the resonances are near any discrete-source frequency and are only weakly damped, one can expect enhanced noise levels. Hein, Koch & Schöberl (2005) computed the low-frequency resonances of a generic three-element high-lift configuration without flow and the computed resonances turned out to be very close to the low-frequency tonal frequencies measured by Pott-Pollenske *et al.* (2003). The resonant frequencies were practically independent of the slat cove geometry, which means that the low-frequency resonances cannot be resonances of the slat cove but are resonances of surface waves. In the literature such surface waves are called Franz-type creeping waves (Überall, Dragonette & Flax 1977), which resonate when exactly n wavelengths fit over the circumference of the whole high-lift configuration. In

Hein *et al.* (2005) we proved the surface wave assertion by numerically computing the resonances of a circular cylinder without flow and compared the computed resonances with the analytic results of Morse & Ingard (1968) for the corresponding diffraction problem.

On the other hand, the slat cove acts like a shallow cavity and the corresponding resonances should scale with the length of the slat cove between slat hook and main wing. To test this hypothesis, we investigate first the resonances of an extended model problem, namely a circular cylinder with a rectangular cutout, finding that the cavity resonances dominate at high frequencies. For our generic high-lift configuration only slight local peaks are observed near the slat cove resonance frequencies in the otherwise fairly flat resonance spectrum. This appears to be due to the more complicated geometry and the slat cavity being open between slat and main wing, which causes higher radiation damping.

The outline of the paper is as follows. After a brief summary of the solution method in § 2, the different physical characteristics of surface-wave resonances and cavity resonances are illustrated for the simple model problem of a circular cylinder with a rectangular cutout in § 3. In § 4, acoustic resonances are computed for a generic high-lift configuration, and the resonances are compared with the low-frequency experimental results of Pott-Pollenske *et al.* (2003). The influence of slat cove parameters on the resonances of a two-element high-lift configuration is investigated in § 5 and a short conclusion completes the paper.

2. Governing equation and perfectly matched layer (PML) boundary condition

The equation governing acoustic disturbances in a medium with zero mean flow is the wave equation. Because of the large spanwise extent of the slat system, the high-lift configuration can be treated as two-dimensional. In the following, all lengths will be non-dimensionalized with a characteristic reference length l^*_{ref}, velocities with the ambient speed of sound c^*_0, densities with the ambient density ρ^*_0, and pressures with $\rho^*_0 c^{*2}_0$. Here the asterisk superscript denotes a dimensional quantity. Assuming periodic time dependence $\exp(-\mathrm{i}\omega^* t^*)$, where ω^* is the circular frequency, the wave equation can be reduced to the Helmholtz equation,

$$\Delta\phi(x, y) + K^2\phi(x, y) = 0, \tag{2.1}$$

for the (non-dimensional) velocity potential $\phi(x, y)$. $\Delta = \partial^2/\partial x^2 + \partial^2/\partial y^2$ is the two-dimensional Laplacian in (non-dimensional) Cartesian coordinates x, y, and $K = \omega^* l^*_{ref}/c^*_0$ denotes the dimensionless frequency, with $K/2\pi$ being the Helmholtz number (Helmholtz 1954). The time-independent dimensionless disturbance velocity and pressure are then given by $\boldsymbol{v}(x, y) = \nabla\phi$ and $p(x, y) = \mathrm{i}K\phi$, respectively. Moreover, we impose the Neumann boundary condition,

$$\frac{\partial\phi}{\partial n} = 0, \tag{2.2}$$

on solid walls.

A complex number K with $\mathrm{Im}(K) < 0$ is called a resonance if there exists a non-trivial solution ϕ to the eigenvalue equation (2.1) satisfying the Neumann boundary condition (2.2) and a radiation condition at infinity as discussed below. It turns out that the eigenfunctions ϕ grow exponentially at infinity. Often resonances are equivalently defined as poles of the meromorphic extension of the resolvent of $-\Delta$ (see Hislop & Sigal 1996; Taylor 1996). To complete our first definition of resonances

it remains to define a radiation condition. For scattering with real $K > 0$, the standard Sommerfeld radiation condition in two dimensions is

$$\lim_{r\to\infty} r^{1/2}\left(\frac{\partial\phi}{\partial r} - \mathrm{i}K\phi\right) = 0, \tag{2.3}$$

but this is no longer a valid characterization of outgoing waves for $\mathrm{Im}(K) < 0$. Alternative formulations of the radiation condition also valid for $\mathrm{Im}(K) < 0$ include complex coordinate stretching (or complex rescaling) (Reed & Simon 1978), the pole condition suggested by Frank Schmidt as discussed in Hohage, Schmidt & Zschiedrich (2003*a*, *b*), series representations, and integral representations.

Numerical computations are necessarily conducted on truncated domains. Without non-reflecting or absorbing boundary conditions at the finite grid boundaries, which approximate the radiation condition at infinity, unphysical reflections at the truncated domain boundary often cause large errors. The perfectly matched layer (PML) absorbing boundary condition of Bérenger (1994) has become increasingly popular in computational electrodynamics as well as in acoustics (see for example Hu 2004). Modelling a physically absorbing layer in Cartesian coordinates, Bérenger (1994) added fictitious damping terms in his split-field Maxwell equations with the remarkable property that no reflections are generated at the interface for all frequencies and angles of wave incidence. It was soon recognized that Bérenger's PML formulation is equivalent to a complex coordinate stretching (Chew & Weedon 1994), which can be interpreted as an analytic continuation of the governing equations into a complex spatial domain (see Chew, Jin & Michielssen 1997; Collino & Monk 1998; Lassas & Somersalo 1998). This can easily be implemented into existing finite-difference or finite-element (FE) codes, and PML formulations in three-dimensional Cartesian, cylindrical or spherical coordinates soon became available. For example, in polar coordinates the complex variable,

$$\rho(r, K) = r + \frac{\mathrm{i}}{K}\sigma(r), \tag{2.4}$$

is introduced instead of r. The damping function $\sigma(r)$ is usually expressed in power form (Hu 2004), smoothly starting at the PML interface $r = r_{PML}$, e.g.

$$\sigma(r) = \begin{cases} \sigma_0\,(r - r_{PML})^{\beta}, & r > r_{PML}, \\ 0, & r \leqslant r_{PML}. \end{cases} \tag{2.5}$$

For a positive (real) damping coefficient $\sigma_0 > 0$ and constant $\beta \geqslant 1$ outgoing waves will decay exponentially in the PML. In numerical computations, the PML can therefore be truncated at $r_{PML} + d_{PML}$, as shown schematically in figure 1 for a typical high-lift configuration with a leading-edge slat with deflection δ_s and a trailing-edge flap with deflection δ_f. Here, d_{PML} denotes the width of the PML, and instead of enforcing (2.3), a Dirichlet boundary condition can be imposed at the outer edge of the PML (Collino & Monk 1998). The error due to artificial reflections at this truncated outer edge of the PML is small if σ_0 and d_{PML} are chosen properly.

For scattering problems, K is a prescribed (real) constant and therefore can be absorbed into the damping coefficient σ_0. Then the above PML formulation is practically identical with the *complex scaling method* of atomic and molecular physics (Hislop & Sigal 1996; Moiseyev 1998). For resonance problems, K is part of the solution and the PML formulation, (2.4), would result in a nonlinear eigenvalue problem with much larger coefficient matrices when solving the problem numerically. Consequently, for the numerical computation of resonances in unbounded space, it is advantageous to use the complex scaling method, i.e. (2.4) without K, see for example

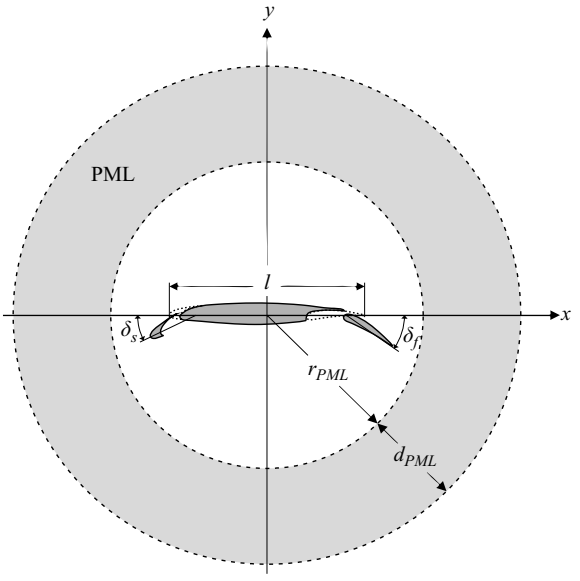

FIGURE 1. Generic three-element high-lift configuration of Pott-Pollenske *et al.* (2003) at landing approach with annular PML.

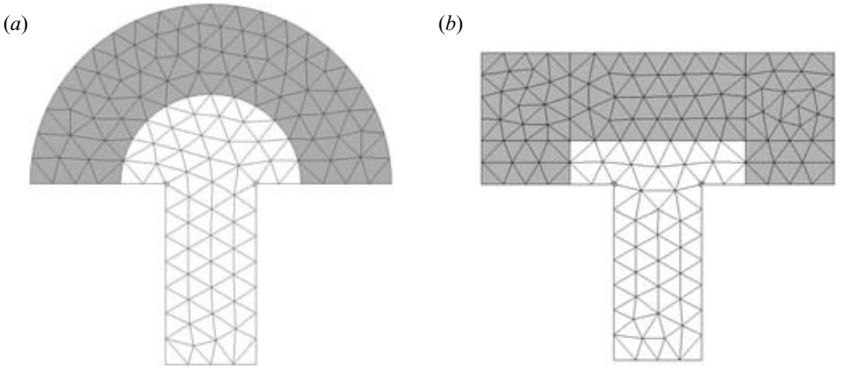

FIGURE 2. Finite-element grids for $l/d = 0.5$ rectangular cavity with $\Delta = 0.3$. (*a*) Annular PML with $r_{PML} = 1$ and $d_{PML} = 1$, (*b*) rectangular PML with $x_{PML} = \pm 1$, $y_{PML} = 0.5$ and $d_{PML} = 1$. The PML is the shaded area.

Hein *et al.* (2004). Then the damping coefficient is no longer constant, but has to be adjusted to the relevant frequency domain.

As mentioned before, the above PML formulation can be easily implemented into existing finite-element codes. For the present paper, we use the high-order finite-element code NGSolve of Joachim Schöberl. Before proceeding with the computation of resonances in open domains with more complicated boundaries we validated our finite-element code by comparing the results for a two-dimensional rectangular open cavity $l/d = 0.5$ with the resonances computed by Koch (2005) which were verified with the classical semi-analytic results of Tam (1976). For this example, we chose the reference length l^*_{ref} to be the cavity length l^* such that $l = 1$. $d = 2$ is then the depth of the cavity for our chosen test example. For $y \geqslant 0$, we apply an annular PML with $r_{PML} = 1$ and $d_{PML} = 1$ and generate a triangulated macro mesh with maximum mesh size $\Delta = 0.3$ using the net generating code NETGEN of Schöberl (1997) (figure 2*a*).

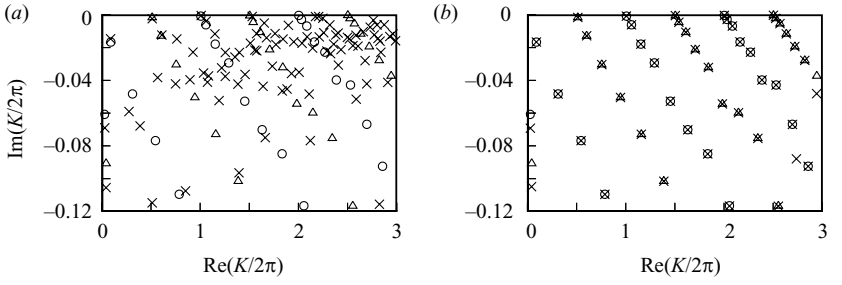

FIGURE 3. Comparison of resonances in a two-dimensional rectangular cavity with $l/d = 0.5$ obtained via the spectral collocation method of Koch (2005)(○, symmetric, △, antisymmetric in x) and via the finite-element method (×) using the mesh of figure 2(*a*) with PML parameters $\sigma_0 = 5$, $\beta = 1$, but differing FE polynomial order p: (*a*) $p = 2$ ($N_{dof} = 721$), (*b*) $p = 12$ ($N_{dof} = 9217$).

Near the singular exit corners of the cavity the grid was adapted locally by geometric mesh refinement (Szabó & Babuška 1991). This means, we cut off the vertex of the triangle at one-eighth of the edge-length. This procedure was repeated several times. The resulting mesh consists of triangles and quadrilaterals.

The computed resonant frequencies are depicted in figure 3(*a*) for low order $p = 2$ and in figure 3(*b*) for high order $p = 12$ of the finite-element method. The open symbols correspond to the results computed by Koch (2005) via the multi-domain spectral collocation method and the crosses represent our present results obtained for the mesh of figure 2(*a*) via the finite-element code NGSolve. This comparison constitutes a severe test for both computations: in the collocation method, a strong formulation with C^1 continuity across the rectangular domain boundaries is employed in conjunction with a rectangular PML, and the eigenvalue problem is solved by a standard eigenvalue problem solver. The variational formulation of the finite-element code requires only C^0 continuity across the triangular mesh elements and uses an annular PML together with a shifted Arnoldi algorithm. Keeping the same mesh, i.e. $\Delta = 0.3$, we vary the order p of the FE polynomial on a triangular element, and hence the number of degrees of freedom N_{dof}. From the spectra shown in figure 3(*a*) with $p = 2$ and figure 3(*b*) with $p = 12$ it is apparent that for the coarse mesh of figure 2(*a*), a high-order finite-element code is a necessity to reach convergence of the results. Other convergence tests include changing the PML parameters or the shift in the Arnoldi method for the numerical solution of the eigenvalue problem. Practically identical results were obtained using the rectangular PML shown in figure 2(*b*) which also demonstrates convergence of the solution.

3. Resonances for a cylinder with a rectangular cutout

After validating our finite-element code NGSolve we investigated the resonances of a simple model problem namely a rigid circular cylinder with a rectangular cavity carved out on one side of the cylinder (figure 4*b*). From this model problem we hope to obtain a deeper insight into the physics behind the resonances of a high-lift configuration. For this model problem, the natural choice for the reference length l^*_{ref} is the diameter D^* of the cylinder, i.e. $K_D = \omega^* D^*/c_0^*$. Without the cavity (figure 4*a*), only resonances of surface waves are possible (Hein *et al.* 2005). By introducing a rectangular cavity of depth d and length l, which we use to model a slat cove, cavity resonances are added which modify these surface-wave resonances. Varying

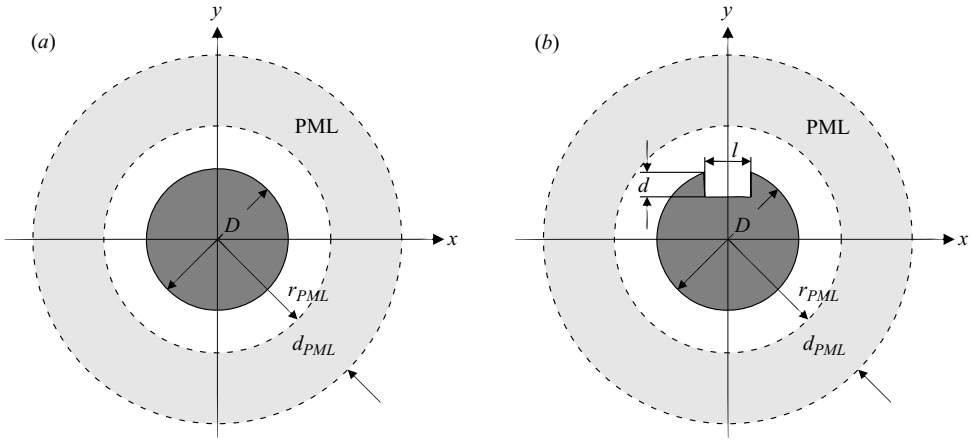

FIGURE 4. (*a*) Solid circular cylinder and (*b*) circular cylinder with a two-dimensional rectangular cavity enclosed by annular PML.

the parameters l/D and l/d, the cavity resonances can be changed over a wide range while the surface-wave resonances remain almost constant. For our results, shown in figure 5 and discussed in the following, we chose $l/D = 1/6$ and $l/d = 2$.

The complex resonances of the surface waves computed for the solid cylinder of figure 4(*a*) are depicted by the solid dots in figure 5(*a*) (the points near the negative imaginary axis represent the discrete approximations of the continuous spectrum and should be disregarded for our present investigation). The classical solution for the pressure $p_s(r, \varphi)$ of an acoustic wave scattered by an infinite rigid cylinder of radius $R = D/2$ can be written down explicitly (Morse & Ingard 1968, p. 400ff),

$$p_s(r, \varphi) = -\hat{p}_i \sum_{n=0}^{\infty} (2 - \delta_{n0})\, i^n \frac{J_n'(kR)}{H_n^{(1)'}(kR)} H_n^{(1)}(kr)\, \cos(n\varphi). \tag{3.1}$$

Here φ is measured from the direction of the incoming plane wave with amplitude $\hat{p}_i$ and propagating in the x-direction, δ_{n0} is Kronecker's delta, $k = \omega^*/c_0^*$ is the wavenumber, J_n is the nth-order Bessel function and $H_n^{(1)}$ is the nth-order Hankel function of the first kind. Complex resonances (also called scattering frequencies) occur at the zeros of $H_n^{(1)'}(z) = 0$ (the so-called nth-Franz zero) which can be computed easily via Newton–Raphson iteration. The first ten zeros ($n = 1, \ldots, 10$) computed this way are marked by the diamond symbols in figure 5(*a*) and agree very well with our numerically computed resonances. In our numerical computation we considered only the half cylinder for $x \geqslant 0$ with Dirichlet or Neumann conditions imposed at the plane $x = 0$. Owing to symmetry, the resonances for the Dirichlet and Neumann problem are equal, i.e. the plotted resonances are double resonances.

In electromagnetic scattering theory, the frequency region when the dimensions of the scattering object are comparable to the wavelength is called the resonance region, and the frequently used canonical model of a perfectly conducting circular cylinder is very similar to our above acoustical model. For this model, Heyman & Felsen (1983) demonstrated the connection between creeping waves and complex resonances. In particular, they showed that the complex resonances can be identified by two indices (m, n), where n marks the angular harmonics and m is associated with the creeping waves. Figure 5(*a*), shows mainly the $m = 1$ branch with the first ten

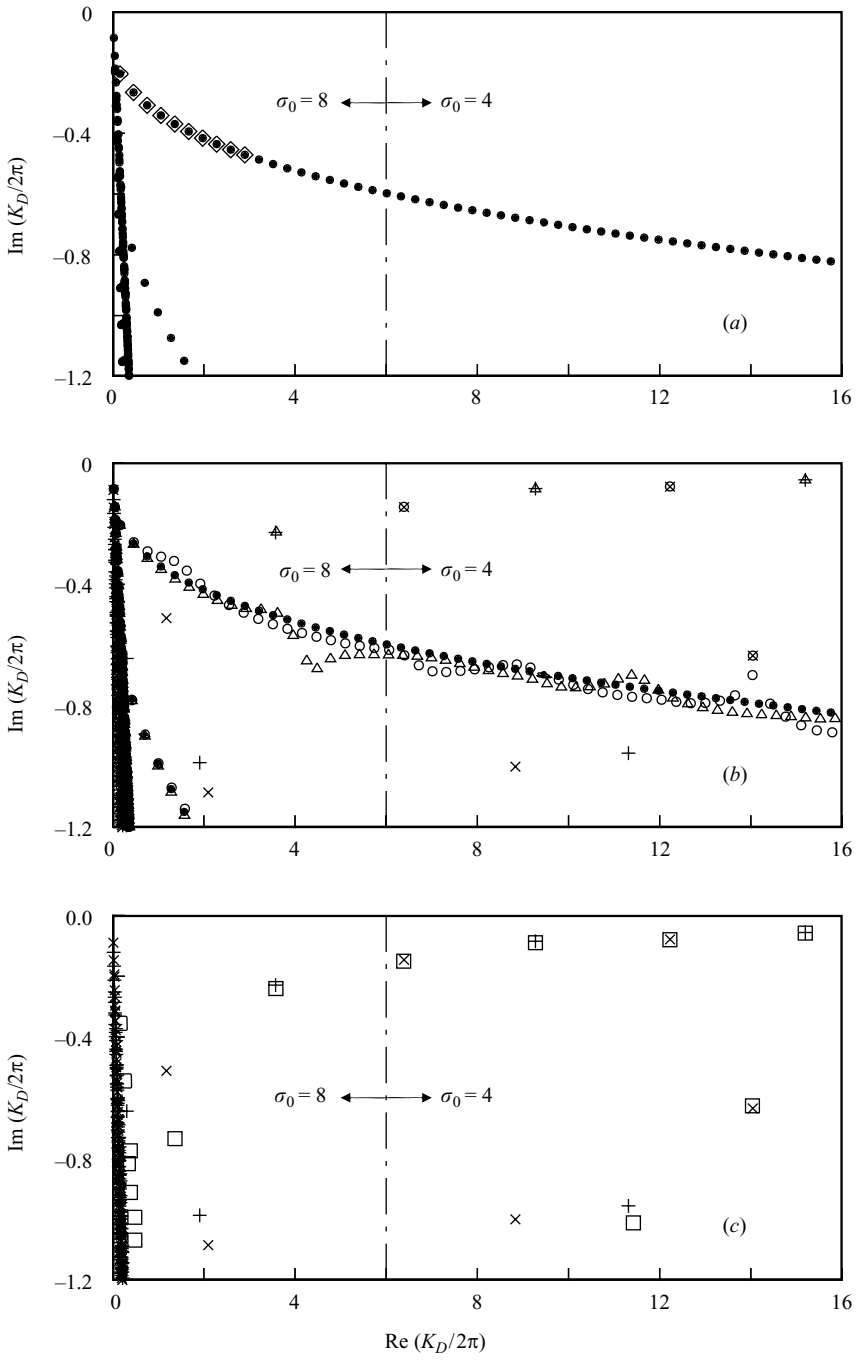

FIGURE 5. (*a*) Surface-wave resonances for a solid circular cylinder: ●, numerical resonances; ◇, first ten zeros of $H_n^{(1)'}(z) = 0$ in (3.1). (*b*) Resonances for a circular cylinder with a two-dimensional rectangular cavity with $l/D = 1/6, l/d = 2$: ○, △, symmetric and antisymmetric resonances; ●, surface-wave resonances replotted from (*a*); ×, +, symmetric and antisymmetric cavity resonances replotted from (*c*). (*c*) Cavity resonances for $l/D = 1/6$, $l/d = 2$: ×, +, symmetric and antisymmetric resonances for cavity on cylinder; □, resonances of Koch (2005) for cavity in half-plane.

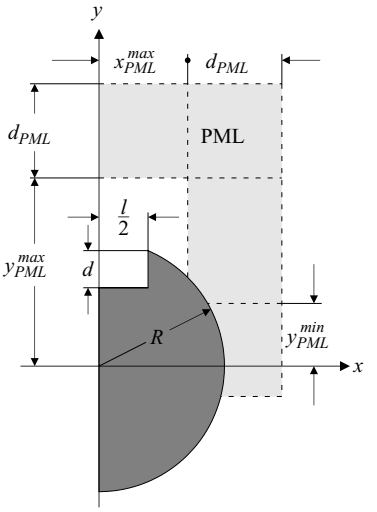

FIGURE 6. Circular cylinder with a two-dimensional rectangular cavity enclosed by rectangular PML.

zeros $n = 1, \ldots, 10$ marked by the diamond symbols, whereas the resonances of the $m = 2$ branch are highly damped and therefore not so important in our acoustical problem.

If the rectangular cavity is added to the cylinder (figure 4*b*), the double resonances of figure 5(*a*) split into symmetric and antisymmetric surface-wave resonances as depicted by the open circles and triangles, respectively, in figure 5(*b*). The few weakly damped symmetric and antisymmetric resonances correspond to cavity resonances. To demonstrate this more clearly we surrounded the cavity with a rectangular PML (figure 6), and computed the corresponding resonances. This way surface-wave resonances are excluded. Again imposing Neumann or Dirichlet conditions at the symmetry plane $x = 0$, we obtained the symmetric and antisymmetric cavity resonances marked by the cross and plus symbols, respectively, in figure 5(*c*). For comparison, we replotted the resonances of Koch (2005) for a rectangular cavity in a half-plane in figure 5(*c*) by the open square symbols. Again, the longitudinal resonances are the least-damped resonances for this shallow cavity with $l/d = 2$, and of the longitudinal cavity resonances only the fundamental resonance is noticeably influenced by the cylinder curvature.

In figure 5, the dash-dotted lines indicate where we patched together two overlapping spectra computed with different PML and Arnoldi shift parameters, i.e. $\sigma_0 = 8$ for $\mathrm{Re}(K_D/2\pi) < 6$, and $\sigma_0 = 4$ for $\mathrm{Re}(K_D/2\pi) \geqslant 6$. For the annular PML we used $r_{PML} = 0.7$, and for the rectangular PML of figure 6 we chose $x_{PML}^{max} = 0.3$, $y_{PML}^{max} = 0.7$. In both cases, the PML thickness was $d_{PML} = 0.5$. The order p of the FE polynomial was $p = 10$, and the maximal mesh size Δ in the above computations was $\Delta = 0.1$.

From figure 5(*b*) we conclude that the resonances of a circular cylinder with a two-dimensional shallow rectangular cavity consist of two types: resonances of the surface waves and cavity resonances with the longitudinal cavity resonances being the least damped resonances. A sequence of resonances with imaginary part tending to zero has to be expected since there exist trapped rays between the sidewalls of the

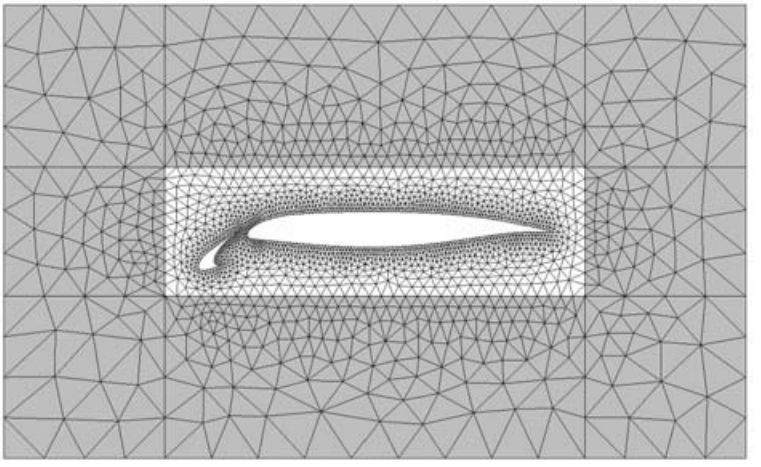

FIGURE 7. Finite-element grid of two-element high-lift configuration with slat angle $\delta_s = 26°$, slat overlap $o_s = -0.018$, slat gap $g_s = 0.0217$ and rectangular PML (shaded region).

rectangular cavity. This was conjectured by Lax & Phillips (1967). For a review of rigorous results on the distribution of resonances we refer to Zworski (1999).

4. Resonances for an airfoil with leading-edge slat

With the insight gained from the model problem, we proceed now with the computation of the acoustic resonances of a two-element high-lift configuration consisting of the main airfoil and a leading-edge slat (figure 7). The geometry is based on the three-element geometry investigated experimentally by Pott-Pollenske *et al.* (2003) with a retracted flap. For our baseline configuration we chose a slat angle $\delta_s = 26°$, a slat overlap $o = -0.018$ and a slat gap $g = 0.0217$ (see figure 15 for the definition of the slat parameters). Now the reference length l^*_{ref} is taken to be the chord length l^* of the clean wing with the slat stowed (cruise condition) (figure 1). Then $K = \omega^* l^*/c_0^*$, and figure 7 shows a typical grid with maximal mesh size $\Delta = 0.1$. To keep the degrees of freedom as low as possible in our finite-element computation, we used a rectangular PML as depicted in figure 7 and refined the grid locally in the slat cove and around the two airfoils.

Following the approach taken for our model problem, we solve the high-lift configuration first with a retracted slat in order to obtain the surface-wave resonances of the high-lift configuration in cruise condition. To avoid the weakly damped whistling tones from the gap between the retracted slat and the main wing, as observed in figure 6 of Hein *et al.* (2005), we eliminate this gap by smoothing the contour (in experiments this is often done with clay). The corresponding surface-wave resonances are depicted in figure 8 up to $\mathrm{Re}(K/2\pi = 20)$. For this we patched together the spectrum from three overlapping spectra with different σ_0 (and Arnoldi shifts) (figure 8). In our finite-element computation, we used the polynomial order $p = 12$. Without the symmetry of our model problem, the double resonances of the circular cylinder in figure 5(*a*) split into two distinct branches starting with a dipole-like eigenfunction similar to that shown by Hein *et al.* (2005) for the symmetric NACA0012 profile. A few of the higher surface-wave eigenfunctions marked (*a*) to (*e*) in figure 8,

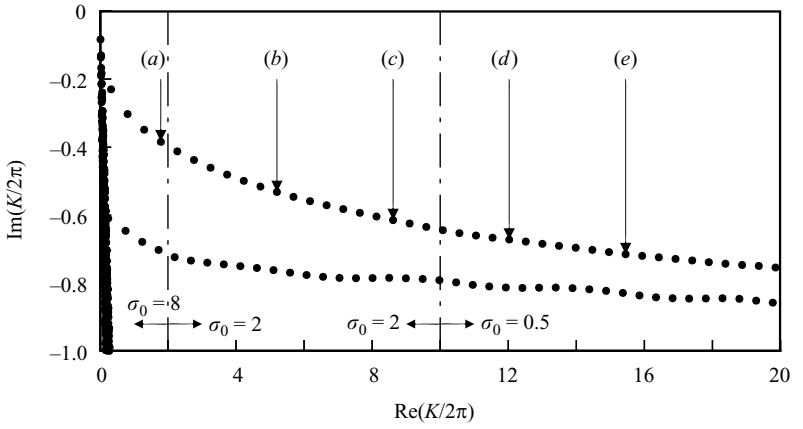

FIGURE 8. Surface-wave resonances (●) for high-lift configuration with retracted slat (clean wing) and rectangular PML: $d_{PML} = 0.5$, $\Delta = 0.1$, $p = 12$. The overlapping spectra are patched together at the dash-dotted lines.

which were chosen near the slat cove resonances in figure 11, are depicted in figure 9. In figure 9 as well as all the other contour plots the real part $\mathrm{Re}(\phi)$ of the complex eigenfunction is plotted and the (darker) maxima are separated from the (lighter) minima by narrow nodal regions. Figure 9 clearly shows the standing surface waves surrounding the airfoil which can be compared with the corresponding eigenfunctions in figure 14 for the airfoil with extracted slat.

Next, we compute the resonances in the slat cove of our baseline configuration with extracted slat and slat angle $\delta_s = 26^\circ$ excluding all surface-wave resonances around the whole wing. This can be achieved by surrounding the extracted slat by an annular PML ending on the main wing as shown in figure 10 where a corresponding grid is depicted. The resulting least-damped resonances are shown in figure 11 together with three sample eigenfunctions. Note that for these slat parameters the least-damped resonances are not the gap modes of Tam & Pastouchenko (2001), but modes which resemble longitudinal cavity modes (Koch 2005), with n nodal lines between slat hook and main wing.

Finally, we consider the high-lift baseline configuration with the slat extracted at a slat angle of $\delta_s = 26^\circ$ (figure 7). Contrary to the clear separation of surface-wave resonances and cavity resonances in our model problem now the slat cove resonances interact strongly with the surface-wave resonances and we obtain the fairly flat resonance spectrum in figure 12. The influence of the slat cove resonances shows up merely as subtle peaks in the resonance spectrum which are marked by arrows in figure 12. Again we patched together the spectrum from three overlapping spectra with different σ_0 as indicated in figure 12 by the dash-dotted lines. The resonances are depicted by open circles. Also included are the surface-wave resonances for the clean wing of figure 8 by solid dot symbols and the slat cove resonances of figure 11 by the star symbols. In general, the resonances of the high-lift configuration with extracted slat have much lower radiation losses than the clean configuration, i.e. more noise is radiated to the far field. Only for very low frequencies do the resonances follow the surface-wave resonances which are essentially independent of slat cove geometry.

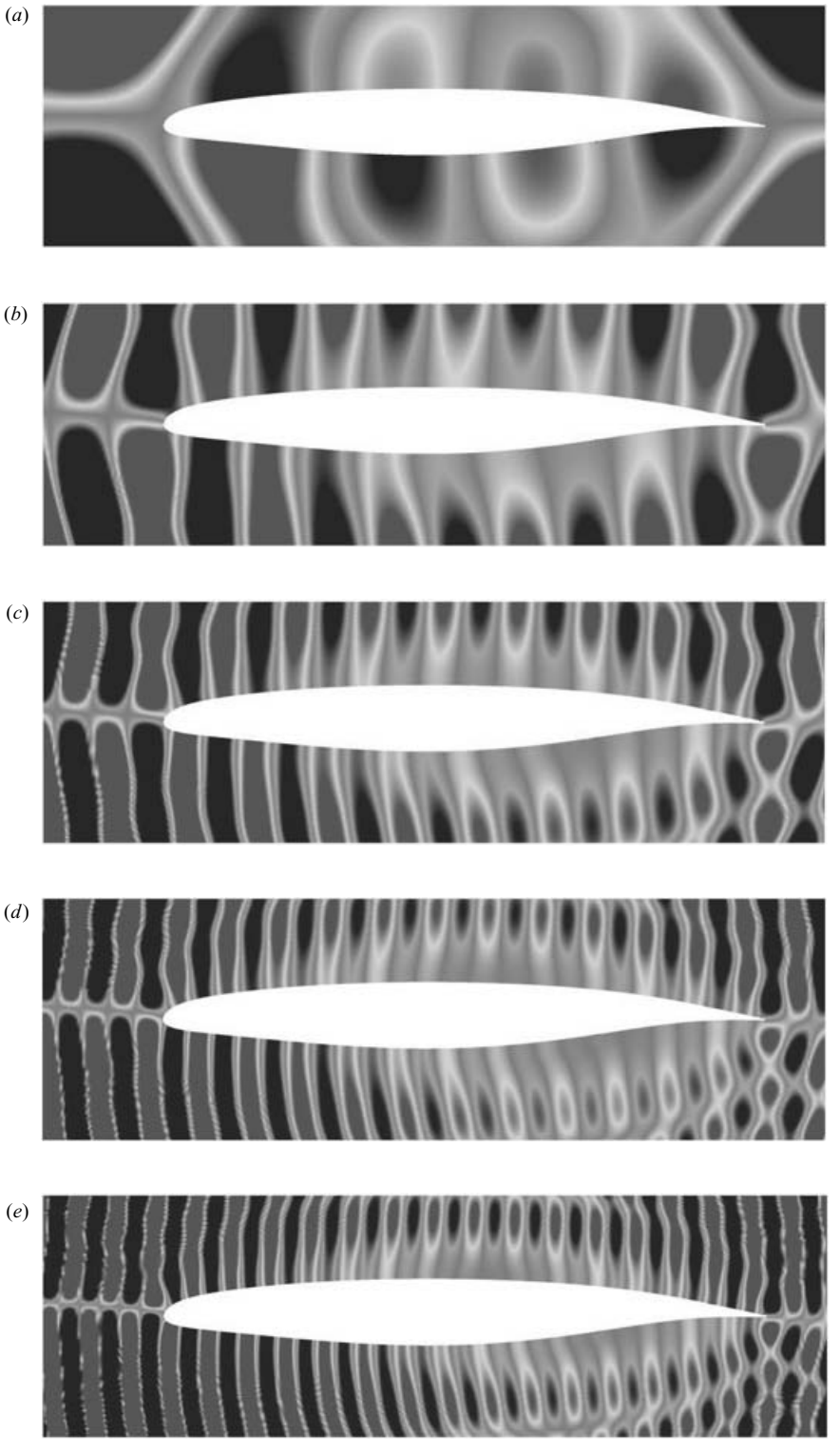

FIGURE 9. Clean wing eigenfunctions Re(ϕ) corresponding to the five surface-wave resonances marked (*a*)–(*e*) in figure 8.

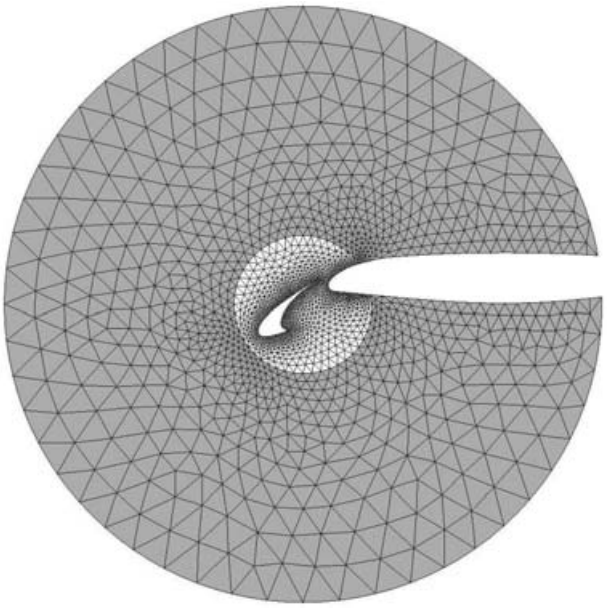

FIGURE 10. Finite-element grid of slat cove with annular PML (shaded region).

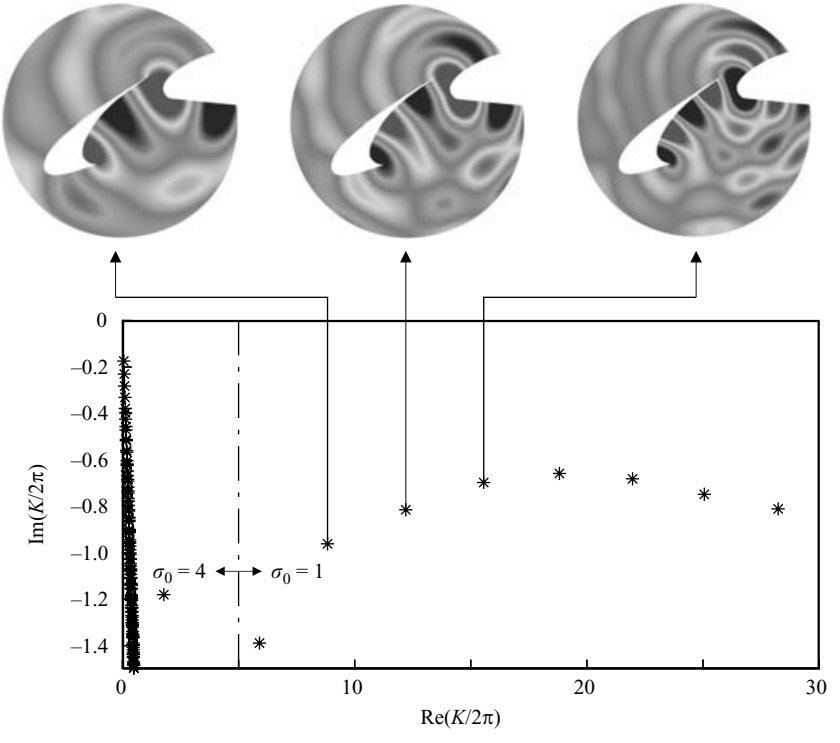

FIGURE 11. Slat cove resonances (*) for high-lift configuration with slat angle $\delta_s = 26^\circ$, slat overlap $o_s = -0.018$, slat gap $g_s = 0.0217$ and annular PML: $d_{PML} = 0.5$, $\sigma_0 = 1$, $\Delta = 0.08$ and $p = 12$. The two overlapping spectra are patched together at the dash-dotted line.

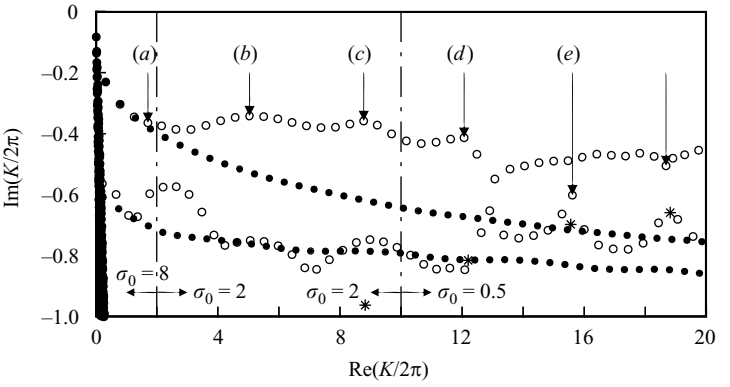

FIGURE 12. Resonances (○) for high-lift configuration with slat angle $\delta_s = 26°$, slat overlap $o_s = -0.018$, slat gap $g_s = 0.0217$ and rectangular PML: $d_{PML} = 0.5$, $\Delta = 0.15$ and $p = 12$. Also included are the surface-wave resonances (●) of the clean wing of figure 8 and the slat cove resonances (*) of figure 11.

For a generic three-element high-lift model with $\delta_s = 26°$ and $\delta_f = 34°$, Pott-Pollenske *et al.* (2003) showed that the experimentally measured spectrum (figure 13*a*) contains distinct frequency peaks at almost constant frequencies for several angles of attack α of the whole high-lift configuration. The high-lift model of Pott-Pollenske *et al.* (2003) had a slat extending over the whole span whereas the trailing-edge flap extended over only half the span. Hein *et al.* (2005) computed the resonances of the three-element model of Pott-Pollenske *et al.* (2003) with the flap extending over the whole span. Here we recomputed the low-frequency resonances for the three-element high-lift configuration without flap. This no-flap configuration consists of the extracted slat and the main wing with wing cove. The results are plotted in figure 13(*b*). The computed dimensional resonant frequencies (in Hz, using $l^* = 0.4\,\mathrm{m}$ and $c_0^* = 340\,\mathrm{m\,s^{-1}}$) are indicated on top of the arrows in figure 13(*b*) and a (dimensional) frequency scale corresponding to that in figure 13(*a*) is added to allow a better comparison. The two-dimensional results in figure 13(*b*) for the no-flap configuration and the two-dimensional results of Hein *et al.* (2005) for the flap extending over the whole span differ, indicating that the influence of three-dimensionality due to the half-span flap in the experiment cannot be neglected. Therefore, a direct comparison of the computed resonant frequencies for the two-dimensional configuration with the measured tones is unrealistic. Nevertheless, the computed resonant frequencies seem to be surprisingly close to the measured frequency peaks despite our no-flow approximation, suggesting that already existing discrete frequency noise sources might be enhanced by acoustic resonances similar to the enhancement of Rossiter modes by cavity resonances (Koch 2005). Also, the peak tone in the experiment of Pott-Pollenske *et al.* (2003) is close to the first slat cove resonance of figure 11.

The slight local peaks in the spectrum marked by arrows in figure 12 occur near the slat cove resonances of figure 11, even though the latter are highly damped. The eigenfunctions corresponding to the first five peaks marked (*a*)–(*e*) in figure 12 are shown in figure 14. In the cove region, the eigenfunctions (*c*), (*d*) and (*e*) of figure 14 agree quite well with the three slat cove eigenfunctions depicted in figure 11. Near $\mathrm{Re}(K/2\pi) = 13$, the two resonance branches seem to interchange in a similar way to the repeated interchanges of the x-symmetric and x-antisymmetric resonances in figure 5(*b*), but it is not clear what that means physically.

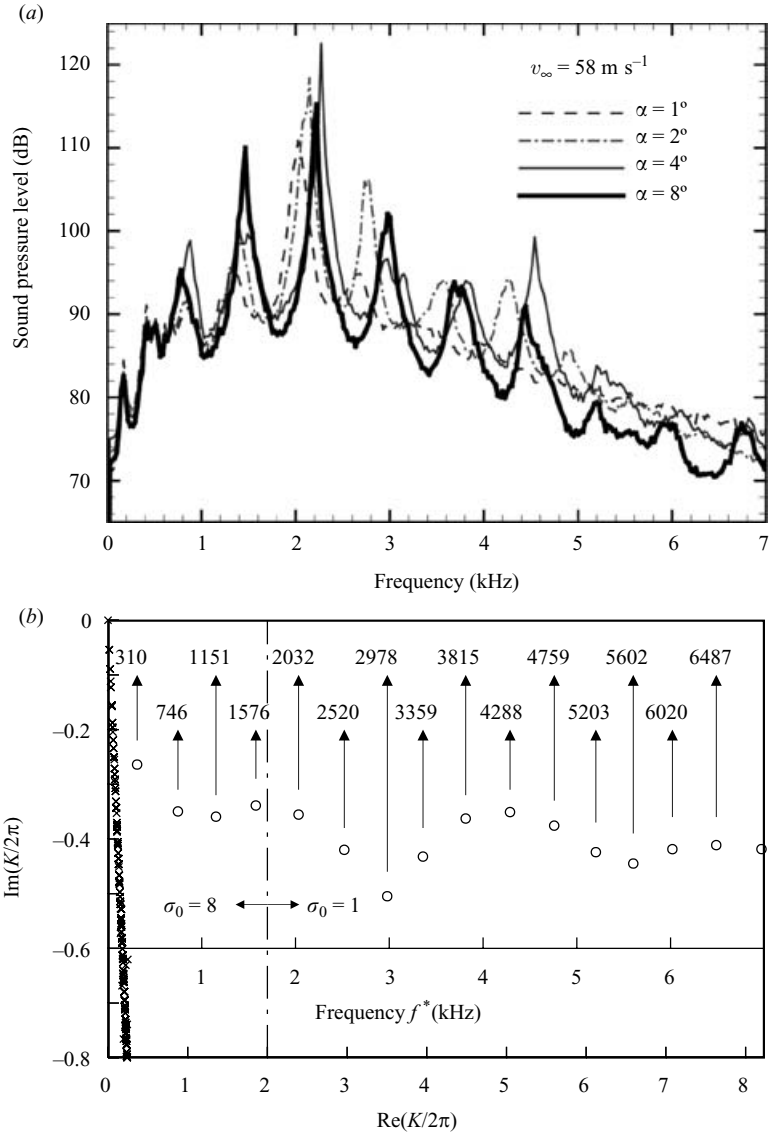

FIGURE 13. Comparison with generic three-element high-lift configuration: (*a*) experimental results (reproduced from Pott-Pollenske *et al.* (2003) with permission of the authors), (*b*) resonance spectrum for high-lift configuration with $\delta_s = 26°$ but without flap ($d_{PML} = 0.5$, $\Delta = 0.1$ and $p = 12$).

5. Variation of resonances with slat cove parameter changes

The traditional geometric parameters determining the aerodynamic performance of leading-edge slats are the slat angle δ_s, the slat overlap o_s and the slat gap g_s (figure 15). Following Pott-Pollenske *et al.* (2003), we used in our baseline configuration the slat cove parameters $\delta_s = 26°$, $o_s = -0.018$, and $g_s = 0.0217$. Hein *et al.* (2005) varied these parameters for the generic three-element high-lift configuration of Pott-Pollenske *et al.* (2003) and found only negligible changes for low-frequency resonances up to $\mathrm{Re}(K/2\pi) = 5$. In the following, we investigate the influence of the slat cove parameters

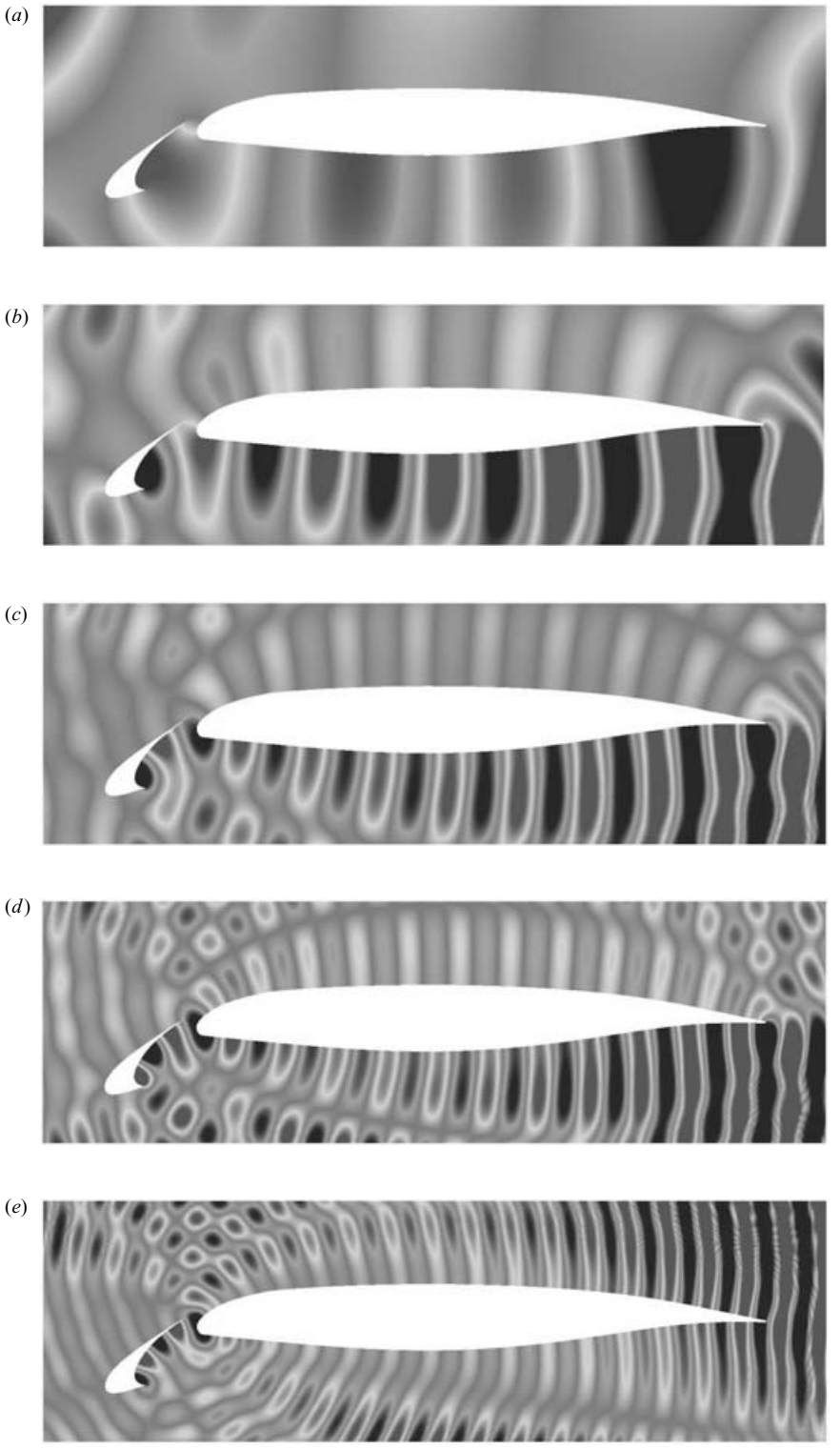

FIGURE 14. High-lift configuration eigenfunctions Re(ϕ) corresponding to the five resonances marked (*a*)–(*e*) in figure 12.

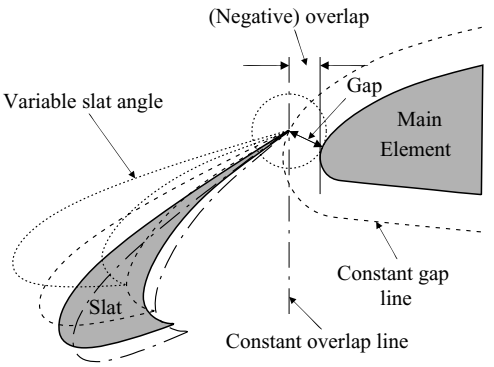

FIGURE 15. Slat cove parameters with $\delta_s = 10°, 20°, 26°$ (shaded baseline configuration) and 30°.

on the high-frequency resonances by extending the frequency range by a factor of four up to $\mathrm{Re}(K/2\pi) = 20$.

First we vary the slat angle δ_s, keeping the slat overlap $o_s = -0.018$ and slat gap $g_s = 0.0217$ fixed. The results for $\delta_s = 10°, 20°$ and 30° are shown in figure 16 complementing figure 12 with $\delta_s = 26°$. We increased the polynomial order up to $p = 14$ and $p = 16$ to check the convergence of the resonances shown and eliminate spurious modes. However, with $p = 16$ we reached the limits of our computational facilities. Again, the subtle peaks in the spectrum are determined by the highly damped slat cove resonances marked by the asterisks in figure 16 which were computed with a similar grid to that shown in figure 10. The complete spectra were computed with a grid similar to that in figure 7 using a rectangular PML. At lower δ_s (figure 16*a*), the slat cove resonances have lower damping at the higher frequencies, resulting in more distinct resonance peaks there; but, in general, the slat cove resonances do not change much by varying δ_s from 10° to 30°. However, Khorrami *et al.* (2000) showed that the self-excited trailing-edge source can change radically with δ_s and this is probably why the highest noise level was observed at the highest slat deflection angle (see also Storms *et al.* 1999).

Next we vary the slat overlap o_s, keeping the slat angle $\delta_s = 26°$ and the slat gap $g_s = 0.0217$ fixed. The resulting spectra for negative and positive slat overlaps are shown in figure 17 complementing figure 12 with $o_s = -0.018$. With increasing (positive) overlap, the slat cove resonances become more damped at higher frequencies, smoothing the corresponding resonant peaks. Slat overlap seems to have a large influence on the slat cove resonances.

Finally, we vary the slat gap g_s, keeping the slat angle $\delta_s = 26°$ and the slat overlap $o_s = +0.005$ fixed. We selected the positive slat overlap $o_s = +0.005$ so that we could let the slat gap g_s go to zero and thereby obtain a closed cavity for comparison even though this case is of no interest for actual high-lift configurations. The resulting spectra are shown in figure 18. For $g_s = 0$ in figure 18(*c*), i.e. a slat cove cavity closed at the slat trailing edge, we see clearly how the longitudinal slat cove resonances dominate the resonance spectrum at higher frequencies. At $\mathrm{Re}(K/2\pi) \approx 17$, the slat cove resonance agrees almost exactly with the weakly damped resonance of the high-lift system similar to our model problem of § 3. From this we conclude that a cavity closed at the bottom has resonances with much lower damping than a cavity with an opening at the cavity bottom. An actual high-lift system has such an opening between

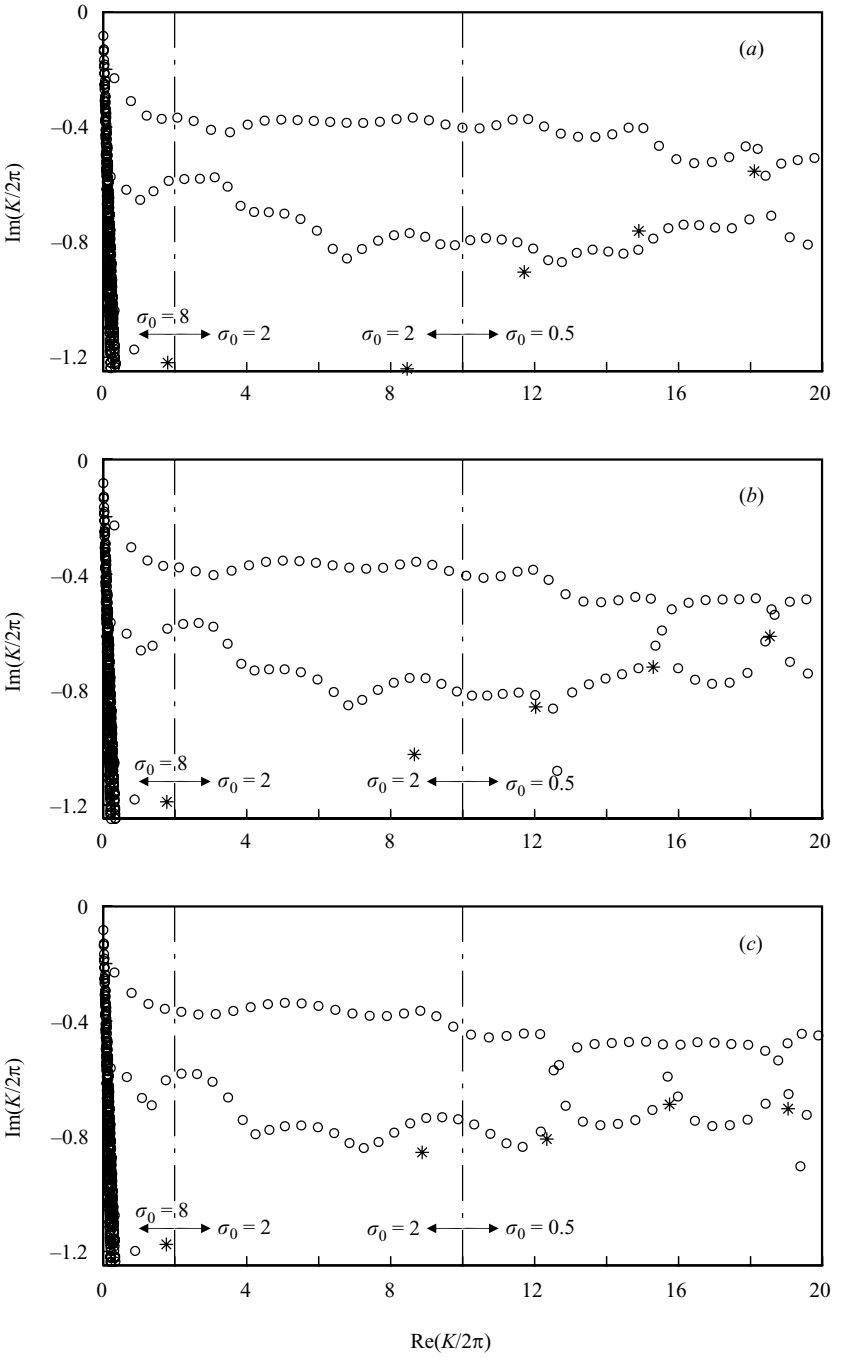

FIGURE 16. Influence of slat angle δ_s on resonances (○) of two-element high-lift configuration with fixed slat overlap $o_s = -0.018$ and fixed slat gap $g_s = 0.0217$ using a rectangular PML: $d_{PML} = 0.5$, $\Delta = 0.15$ and $p = 16$. (*) denotes the slat cove resonances. (*a*) $\delta_s = 10°$, (*b*) $\delta_s = 20°$, (*c*) $\delta_s = 30°$.

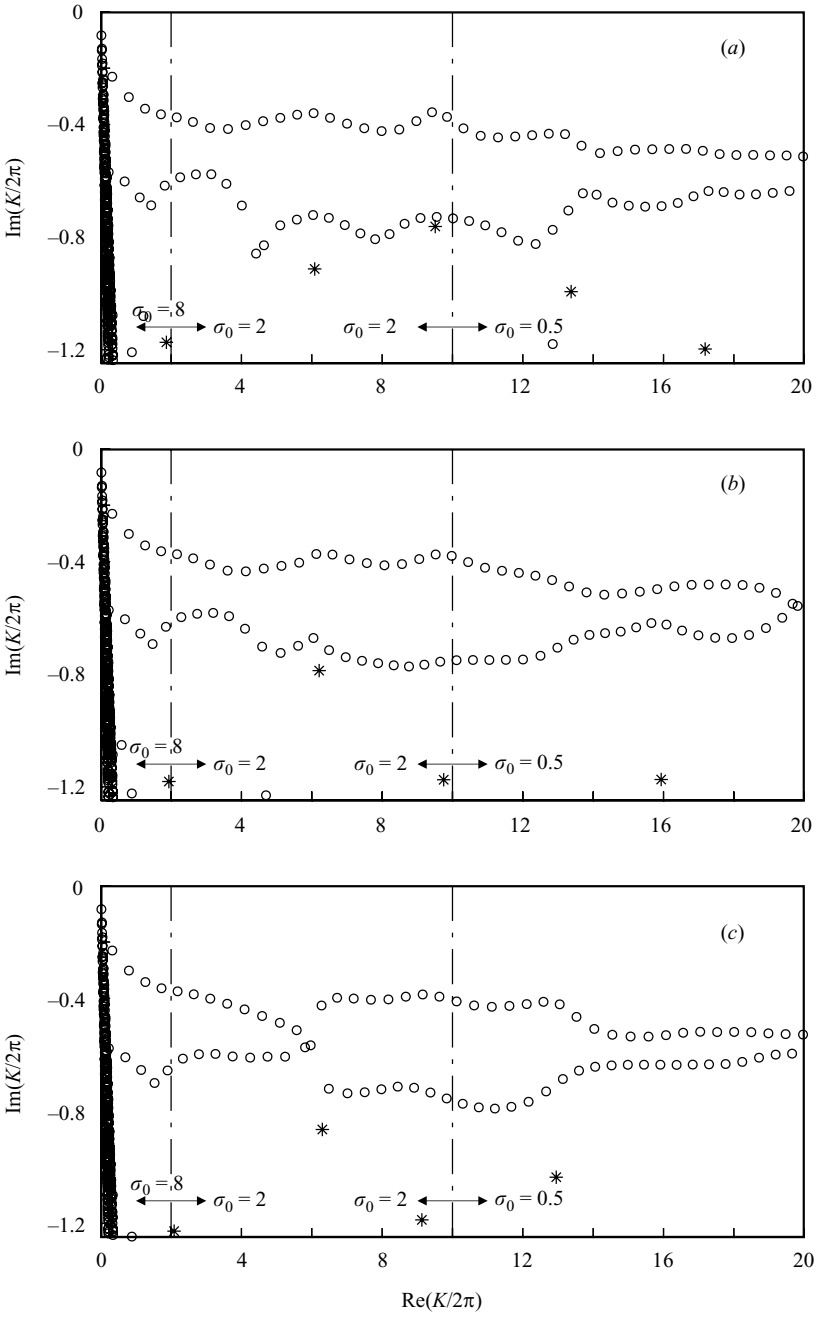

FIGURE 17. Influence of slat overlap o_s on resonances (○) of two-element high-lift configuration with fixed slat angle $\delta_s = 26^\circ$ and fixed slat gap $g_s = 0.0217$ using a rectangular PML: $d_{PML} = 0.5$, $\Delta = 0.15$ and $p = 16$. (*) denotes the slat cove resonances. (*a*) $o_s = -0.005$, (*b*) $o_s = +0.005$, (*c*) $o_s = +0.02$.

the slat trailing edge and the main wing and therefore shows higher damping than our model problem. However, the effect of mean flow through such an opening still has to be assessed.

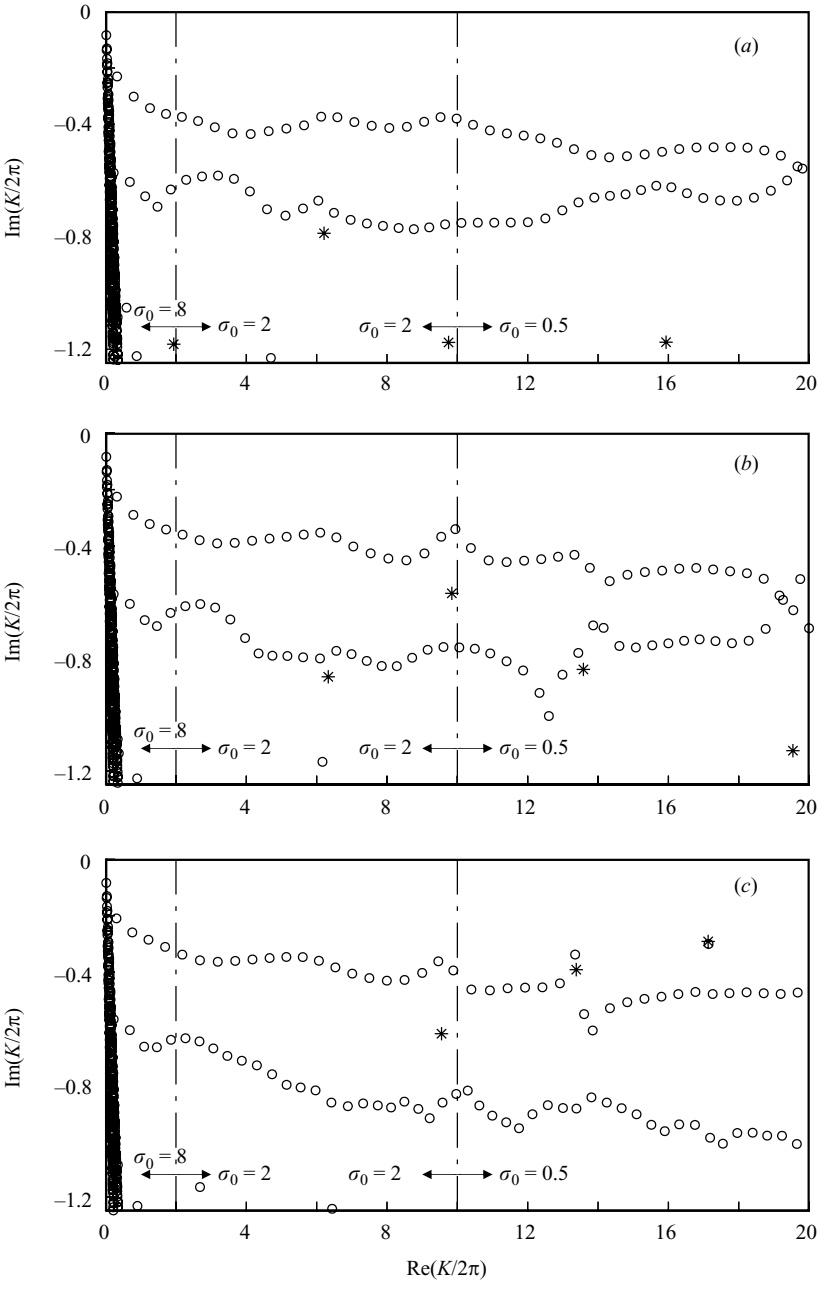

FIGURE 18. Influence of slat gap g_s on resonances (○) of two-element high-lift configuration with fixed slat angle $\delta_s = 26^\circ$ and fixed slat overlap $o_s = +0.005$ using a rectangular PML: $d_{PML} = 0.5$, $\Delta = 0.15$ and $p = 16$. * denotes the slat cove resonances. (*a*) $g_s = 0.0217$, (*b*) $g_s = 0.01$, (*c*) $g_s = 0$.

6. Conclusion

We computed acoustic resonances of a generic two-element high-lift configuration with a single leading-edge slat. These resonances are damped by radiation losses to infinity, but could possibly enhance coherent slat noise sources observed in small-scale

low-Reynolds-number experiments. For the computation of the acoustic resonances we neglected mean flow effects, assuming that mean flow is not important at the low Mach numbers of aircraft landing and approach. However, for the exciting shear-layer sources, mean flow is essential. To avoid unphysical reflections at the truncated domain boundaries we employed perfectly matched layer boundary conditions in the form of the complex scaling method of atomic and molecular physics.

Studying first the simple model of a circular cylinder with a rectangular cutout, we demonstrated the existence of two distinct types of resonance: the first type of resonance is due to surface waves and scales with the total circumference, i.e. the airfoil length. The second type of resonance corresponds to longitudinal resonances in a cavity and scales with the length of the cavity. For our model problem, the weakly damped longitudinal cavity resonances dominate the resonance spectrum and are expected to considerably enhance discrete frequency sources if their frequency is close to these cavity resonances. Similar types of resonance are found in our generic high-lift system. However, in the high-lift system, the cavity resonances are much more damped owing to the opening between the slat trailing edge and the main wing, and these exist as local peaks only slightly above the surface-wave resonances in the otherwise fairly flat frequency spectrum. These longitudinal cavity resonances of the slat cove between the slat hook and the main wing are much less damped than the transverse gap resonances of Tam & Pastouchenko (2001) and Agarwal & Morris (2002) between the slat trailing edge and the main wing. Varying the slat parameters, we showed that the slat cove geometry, in particular the slat overlap and the slat gap, have a strong influence on the resonances and therefore on the response to coherent noise sources in a high-lift system.

We are grateful to the three referees for their valuable suggestions. In particular, the constructive criticism of one referee concerning the non-existence of coherent slat noise sources in real aircraft led to considerable improvements of our paper. In this context we gratefully acknowledge helpful advice from M. Choudhari and W. Dobrzynski.

REFERENCES

Agarwal, A. & Morris, P. 2002 Investigation of the physical mechanisms of tonal sound generation by slats. *AIAA Paper* 2002-2575.

Andreou, C., Graham, W. & Shin, H.-C. 2006 Aeroacoustic study of airfoil leading edge high-lift devices. *AIAA Paper* 2006-2515.

Bérenger, J. 1994 A perfectly matched layer for the absorption of electromagnetic waves. *J. Comput. Phys.* **114**, 185–200.

Chew, W. & Weedon, W. 1994 A 3-D perfectly matched medium from modified Maxwell's equation with stretched coordinates. *Microwave Optical Technol. Lett.* **7** (13), 599–604.

Chew, W., Jin, J. & Michielssen, E. 1997 Complex coordinate stretching as a generalized absorbing boundary condition. *Microwave Optical Technol. Lett.* **15** (3), 144–147.

Choudhari, M. & Khorrami, M. 2006 Slat cove unsteadiness: effect of 3D flow structure. *AIAA Paper* 2006-0211.

Collino, F. & Monk, P. 1998 The perfectly matched layer in curvilinear coordinates. *SIAM J. Sci. Comput.* **19**, 2061–2090.

Crighton, D. 1991 Airframe noise. In *Aeroacoustics of Flight Vehicles: Theory and Practice. Vol. 1: Noise Sources* (ed. H. H. Hubbard), pp. 391–447. NASA.

Czech, M., Crouch, J., Stoker, R., Strelets, M. & Garbaruk, A. 2006 Cavity noise generation for circular and rectangular vent holes. *AIAA Paper* 2006-2508.

Davy, R., Moens, F. & Remy, H. 2002 Aeroacoustic behaviour of a 1/11 scale Airbus model in the open anechoic wind tunnel CEPRA 19. *AIAA Paper* 2002-2412.

Deck, S. 2005 Zonal-detached-eddy simulation of the flow around a high-lift configuration. *AIAA J.* **43**, 2372–2384.

Dobrzynski, W. & Pott-Pollenske, M. 2001 Slat noise source studies for farfield noise prediction. *AIAA Paper* 2001-2158.

Dobrzynski, W., Nagakura, K., Gehlhar, B. & Buschbaum, A. 1998 Airframe noise studies on wings with deployed high-lift devices. *AIAA Paper* 98-2337.

Dobrzynski, W., Gehlhar, B. & Buchholz, H. 2001 Model and full scale high-lift wing wind tunnel experiments dedicated to airframe noise reduction. *Aerosp. Sci. Technol.* **5**, 27–33.

Fischer, M., Friedel, H., Holthusen, H., Gölling, B. & Emunds, R. 2006 Low noise design trends derived from wind tunnel testing on advanced high-lift devices. *AIAA Paper* 2006-2562.

Grosche, F.-R., Schneider, G. & Stiewitt, H. 1997 Wind tunnel experiments on airframe noise sources of transport aircraft. *AIAA Paper* 97-1642.

Guo, Y. 1997 A model for slat noise generation. *AIAA Paper* 97-1647.

Hayes, J., Horne, W., Soderman, P. & Bent, P. 1997 Airframe noise characteristics of a 4.7% scale DC-10 model. *AIAA Paper* 97-1594.

Hein, S., Hohage, T. & Koch, W. 2004 On resonances in open systems. *J. Fluid Mech.* **506**, 255–284.

Hein, S., Koch, W. & Schöberl, J. 2005 Acoustic resonances in a 2D high lift configuration and a 3D open cavity. *AIAA Paper* 200-2867.

Helmholtz, H. 1954 *On the Sensations of Tone*, 2nd edn. Dover.

Heyman, E. & Felsen, L. 1983 Creeping waves and resonances in transient scattering by smooth convex objects. *IEEE Trans. Antennas Propagat.* **31**, 426–437.

Hislop, P. & Sigal, I. 1996 *Introduction to Spectral Theory*. Springer.

Hohage, T., Schmidt, F. & Zschiedrich, L. 2003*a* Solving time-harmonic scattering problems based on the pole condition. I: Theory. *SIAM J. Math. Anal.* **35**, 183–210.

Hohage, T., Schmidt, F. & Zschiedrich, L. 2003*b* Solving time-harmonic scattering problems based on the pole condition. II: Convergence of the PML method. *SIAM J. Math. Anal.* **35**, 547–560.

Horne, W., James, K., Arledge, T., Soderman, P., Burnside, N. & Jaeger, S. 2005 Measurements of 26%-scale 777 airframe noise in the NASA Ames 40 by 80 foot wind tunnel. *AIAA Paper* 2005-2810.

Hu, F. 2004 Absorbing boundary conditions. *Intl J. Comput. Fluid Dyn.* **18**, 513–522.

Jenkins, L., Khorrami, M. & Choudhari, M. 2004 Characterization of unsteady flow structures near leading-edge slat: Part I. PIV measurements. *AIAA Paper* 2004-2801.

Kaepernick, K., Koop, L. & Ehrenfried, K. 2005 Investigation of the unsteady flow field inside a leading edge slat cove. *AIAA Paper* 2005-2813.

Khorrami, M. 2003 Understanding slat noise sources. In *Proc. EUROMECH Colloquium 449, Computational Aeroacoustics: From Acoustic Sources Modeling to Far-Field Radiated Noise Prediction, Chamonix, France*.

Khorrami, M., Berkman, M. & Choudhari, M. 2000 Unsteady flow computations of a slat with a blunt trailing edge. *AIAA J.* **38**, 2050–2058.

Khorrami, M., Singer, B. & Berkman, M. 2002*a* Time-accurate simulations and acoustic analysis of slat free-shear layer. *AIAA J.* **40**, 1284–1291.

Khorrami, M., Singer, B. & Lockard, D. 2002*b* Time-accurate simulations and acoustic analysis of slat free-shear layer: Part II. *AIAA Paper* 2002-2579.

Khorrami, M., Choudhari, M. & Jenkins, L. 2004 Characterization of unsteady flow structures near leading-edge slat: Part II. 2D computations. *AIAA Paper* 2004-2802.

Koch, W. 2005 Acoustic resonances in rectangular open cavities. *AIAA J.* **43**, 2342–2349.

Lassas, M. & Somersalo, E. 1998 On the existence and convergence of the solution of PML equations. *Computing* **60**, 229–241.

Lax, P. & Phillips, R. 1967 *Scattering Theory*. Academic.

Michel, U., Barsikow, B., Helbig, J., Hellmig, M. & Schüttepelz, M. 1998 Flyover noise measurements on landing aircraft with a microphone array. *AIAA Paper* 98-2336.

Moiseyev, N. 1998 Quantum theory of resonances: calculating energies, widths and cross-sections by complex scaling. *Phys. Rep.* **302**, 211–293.

Morse, P. & Ingard, K. 1968 *Theoretical Acoustics*. McGraw-Hill.

Oerlemans, S. & Sijtsma, P. 2004 Acoustic array measurements of a 1:10.6 scaled Airbus A340 model. *AIAA Paper* 2004-2924.

Olson, S., Thomas, F. & Nelson, R. 2000 A preliminary investigation into slat noise production mechanisms in high-lift configuration. *AIAA Paper* 2000-4508.

Olson, S., Thomas, F. & Nelson, R. 2001 Mechanisms of slat noise production in a 2D multi-element airfoil configuration. *AIAA Paper* 2001-2156.

Piet, J., Michel, U. & Böhning, P. 2002 Localization of the acoustic sources of the A340 with a large phased microphone array during flight tests. *AIAA Paper* 2002-2506.

Pott-Pollenske, M., Alvarez-Gonzalez, J. & Dobrzynski, W. 2003 Effect of slat gap on farfield noise and correlation with local flow characteristics. *AIAA Paper* 2003-3228.

Reed, M. & Simon, B. 1978 *Methods of Modern Mathematical Physics IV*. Academic.

Roger, M. & Pèrennés, S. 2000 Low-frequency noise sources in two-dimensional high-lift devices. *AIAA Paper* 2000-1972.

Rossiter, J. 1964 Wind-tunnel experiments on the flow over rectangular cavities at subsonic and transonic speeds. *ARC R.&M*. 3438.

Schöberl, J. 1997 NETGEN An advancing front 2D/3D-mesh generator based on abstract rules. *Comput. Visualiz. Sci.* **1**, 41–52.

Singer, B., Lockard, D. & Brentner, K. 2000 Computational aeroacoustic analysis of slat trailing-edge flow. *AIAA J.* **38**, 1558–1564.

Soderman, P., Kafyeke, F., Burnside, N., Chandrasekharan, R., Jaeger, S. & Boudreau, J. 2002 Aerodynamic noise induced by laminar and turbulent boundary layers over rectangular cavities. *AIAA Paper* 2002-2406.

Stoker, R., Guo, Y., Street, C. & Burnside, N. 2003 Airframe noise source locations of a 777 aircraft in flight and comparisons with past model scale tests. *AIAA Paper* 2003-3232.

Storms, B., Hayes, J., Moriarty, P. & Ross, J. 1999 Aeroacoustic measurements of slat noise on a three-dimensional high-lift system. *AIAA Paper* 99-1957.

Szabó, B. & Babuška, I. 1991 *Finite Element Analysis*. Wiley.

Takeda, K., Ashcroft, G., Zhang, X. & Nelson, P. 2001 Unsteady aerodynamics of slat cove flow in a high-lift device configuration. *AIAA Paper* 2001-0706.

Takeda, K., Zhang, X. & Nelson, P. 2002 Unsteady aerodynamics and aeroacoustics of a high-lift device configuration. *AIAA Paper* 2002-0570.

Takeda, K., Zhang, X. & Nelson, P. 2004 Computational aeroacoustic simulations of leading-edge slat flow. *J. Sound Vib.* **270**, 559–572.

Tam, C. 1976 The acoustic modes of a two-dimensional rectangular cavity. *J. Sound Vib.* **49**, 353–364.

Tam, C. & Pastouchenko, N. 2001 Gap tones. *AIAA J.* **39**, 1442–1448.

Taylor, M. 1996 *Partial Differential Equations II*, Springer.

Terracol, M., Labourasse, E., Manoha, E. & Sagaut, P. 2003 Simulation of the 3D unsteady flow in a slat cove for noise prediction. *AIAA Paper* 2003-3234.

Überall, H., Dragonette, L. & Flax, L. 1977 Relation between creeping waves and normal modes of vibration of a curved body. *J. Acoust. Soc. Am.* **61**, 711–715.

Zworski, M. 1999 Resonances in physics and geometry. *Not. AMS* **46**, 319–328.